

Vacancy assisted solute transport mechanisms responsible for the solute atom agglomeration during the early stages of aging in Al-Cu-based alloys

M. A. Quiroga , C. Macchi , and A. Somoza ^{*}

Instituto de Física de Materiales Tandil (IFIMAT, UNCPBA) and Centro de Investigaciones en Física e Ingeniería del Centro de la Provincia de Buenos Aires (CIFICEN, UNCPBA-CICPBA-CONICET), Pinto 399, B7000GHG Tandil, Argentina



(Received 19 August 2021; accepted 23 February 2022; published 11 March 2022)

An approach using combined results, obtained by different experimental variants of positron annihilation spectroscopy and from kinetic Monte Carlo simulations, made it possible to determine the fundamental mechanisms by which vacancies assist solute atoms to form clusters during the earliest stages of precipitation kinetics in age-hardenable Al-Cu and Al-Cu-Mg alloys. The investigations were performed on the conventional precipitation-hardening system Al-1.74Cu (at. %) alloy aged at 293 and 342 K; these temperatures were chosen since they are low enough to avoid the formation of more stable nanostructures. To understand the influence of a minor alloying element on the solute clustering, the ternary Al-1.74Cu-0.35Mg (at. %) alloy was also studied. Interpreted in terms of the so-called vacancy pump model of solute aggregation, the results obtained made it possible to give a detailed and precise description concerning the role of the solute-vacancy exchanges in the solute clustering dynamics and the energetic stabilization of the formed clusters. It deserves to be pointed out that the results of our simulations for the ternary alloy indicate that, when aging proceeds, the solute atoms transported by vacancies progressively form Cu-Mg coclusters containing different amounts of nonmixed Cu or Mg solute atoms.

DOI: [10.1103/PhysRevMaterials.6.033603](https://doi.org/10.1103/PhysRevMaterials.6.033603)

I. INTRODUCTION

Age hardening is a well-known thermal treatment for particular groups of aluminum alloys to achieve optimal mechanical properties. The technological importance of age hardening has stimulated an intense research effort since its discovery at the beginning of the last century. The decomposition, that is, the structural evolution of an alloy, is a complicated phenomenon controlled by thermodynamical factors (phase stability) as well as atomistic processes (solute transport). It is worth mentioning that the basic requirement for an alloy to be amenable to age hardening is a decrease in solid solubility of one or more of the solute elements with decreasing temperature. A detailed description of the sequence of the thermal treatments involved in the different stages of the kinetic decomposition of an age-hardenable alloy is given in Ref. [1]. Variations in this sequence strongly depend on the composition of the system and the sequence of thermal treatments.

The latest investigations of Al-based age-hardenable alloys, mainly Al-Cu- and Al-Zn-based alloys, have been focused on the earliest stages of decomposition of the supersaturated solid solution (SSSS) since this is a crucial step for determining the final microstructure of the alloy. During the mentioned aging stages, the microstructure of the alloy evolves by progressive formation of coherent solute aggregates (usually named solute clusters) and metastable Guinier-Preston (GP) zones at later stages. It is

now well accepted that solute-vacancy association is one of the fundamental processes controlling precipitation hardening phenomena in this kind of alloy [1,2]. For Al-Cu alloys, the addition of Mg can have the apparently unique effect of promoting rapid early hardening after quenching [usually to room temperature (RT)] and aging at intermediate temperatures such as 100 to 200 °C. Results obtained using one of the most advanced imaging techniques at the atomic scale, atom probe, in its evolving variants [atom probe field ion microscopy, three-dimensional atom probe (3DAP), and atom probe tomography] [3,4], have shown that this effect is caused by the rapid formation of solute clusters in a matter of seconds, which is known in the literature as *cluster hardening*. It was also reported that this process is slower for lower aging temperatures.

Vacancies play a fundamental role not only in the transport of the solute atoms but also by contributing to the energetic balance of the phases in which they are included as structural constituents. Since aging treatments are normally carried out at temperatures low enough to avoid significant production of vacancies in thermal equilibrium, nonequilibrium vacancies such as quenched-in vacancies, or produced by cold work are especially important [1]. However, vacancies are an elusive component of any alloy, not only due to their low concentration but also because they cannot be imaged by any type of microscopy, even at atomic resolution.

Positron annihilation spectroscopy (PAS) has proved to be the most sensitive experimental technique for detecting vacancylike defects and their role during structural transformations in alloys [5,6]. Different experimental variants of this nuclear spectroscopic technique have been widely applied to

^{*}Corresponding author: asomoza@exa.unicen.edu.ar

study the role of vacancies in the aging behavior of aluminum age-hardenable alloys. First, positron annihilation lifetime spectroscopy (PALS) and Doppler broadening spectroscopy (DBS) were used to study the formation of GP zones in Al-Zn alloys [7]. At the beginning of this century, another variant of PAS called *coincidence Doppler broadening spectroscopy* (CDBS) demonstrated to be particularly useful for identifying the nature of the solute atoms in contact with vacancylike defects in precipitates [8–12]. These techniques have been used to obtain information on the decomposition kinetics of the alloys through the presence of vacancylike defects inside the decomposition products, that is, solute-vacancy clusters and the chemical composition of the clusters and nanoparticles formed. Dlubek [13] and Krause *et al.* [14] published comprehensive review papers on the decomposition kinetics of Al-based age-hardenable alloys. Critical reviews of this kind of subject can be found in Refs. [5,6,15,16]. Especially PALS and CDBS have contributed to the understanding of the effects of adding a microaddition of silver on the precipitation process in Al-Cu-Mg alloys with low [17] or high Mg:Cu ratios [18]. Both positron techniques have also been successfully applied to investigate precipitation kinetics in several prepared Al-based age-hardenable alloys as well as in some commercial alloys [19–26].

In the early 1960s, a type of Monte Carlo algorithm called *kinetic Monte Carlo* (kMC) was developed to describe the time evolution of different systems of interest for many fields of physics and chemistry [27]. It is important to point out that kMC is a simulation technique which can bring insights into the physicochemical properties of a solid at the nano and subnanometric scale in kinetic processes evolving in a wide time range, from picoseconds until several hours [28–31].

Regarding the use of kMC, in a recent overview, the state-of-the-art in the understanding of precipitation kinetics phenomena in metallic alloys is carefully described ([32] and references therein). Previously, different authors reported kMC studies on Al-based age-hardenable alloys, which are directly related to the scope of this paper. Sha and Cerezo [33] employed kMC to model the early stages of precipitation kinetics in an Al-Zn-Mg-Cu alloy, specifically the formation and growth of solute clusters. These authors compared simulated results with those experimentally obtained using 3DAP. De Geuser *et al.* [34] used kMC simulations parametrized with CALPHAD thermodynamic databases to study the solute clustering process in the early stages of the artificial aging at intermediate temperatures in the binary Al-1.7Cu (at. %) alloy. Liang *et al.* [35] studied the solute clustering in the Al-0.57Mg-0.77Si (at. %) alloy.

The present investigation was carried out to obtain a deeper level of understanding about the role of vacancies in the mechanisms responsible for the transport of solute atoms to the formation and growth of solute clusters during the earliest aging stages of the SSSS kinetic precipitation of two Al-Cu-based alloys. First, we have studied the binary Al-1.74Cu (at. %), equivalent to Al-4Cu (wt. %), because it is widely considered by the metallurgical community a model age-hardenable alloy. Additionally, the ternary Al-1.74Cu-0.35Mg (at. %), equivalent to Al-4Cu-0.3Mg (wt. %), was studied to understand how the addition of Mg as a third alloying element

to the binary alloy influences the solute clustering process responsible for the rapid early hardening effect described above.

In that sense, PALS [17,21] and CDBS [8] experimental data previously reported were fitted using an improved model to analyze the positron data that made it possible to gain information regarding the sites in which positrons become trapped and annihilated. On the other hand, we have used kMC as the most appropriate modeling technique to describe the mechanisms involved in the transport of solute atoms assisted by vacancies to the formation and growth of solute clusters and how the solute-vacancy interaction occurs. This paper constitutes a leading case in search of a detailed description of the most fundamental mechanisms operating during the solute agglomeration process mediated by vacancies induced by thermal treatments.

This paper is organized as follows. In Sec. II, the key elements are given to understand the implementation of a kMC algorithm to study the atomic diffusion processes in a crystal lattice assisted by vacancies. In this section, details on the specific code developed to carry out the kMC computer simulations of solute atom transport in a crystal lattice and the solute-vacancy interactions are also described. Section III A is devoted to analyzing and discussing PALS and CDBS results. In Sec. III B, results of kMC simulations are presented. In Sec. IV, an overall discussion of the experimental and simulated kMC results presented in Secs. III A and III B is given. Finally, in Sec. V, the key results obtained in this paper are presented.

II. METHODOLOGY

To study the atomic transport process in a crystal lattice assisted by vacancies, a kMC algorithm was implemented. Under this frame, kMC can simulate the crystal state-to-state evolution in time where a kMC trajectory consists of a stochastic sequence of discrete jumps from one system state to another one. Specifically, each system state is defined by a given atomic configuration in the crystal lattice. To calculate the energy of a given state, the following Hamiltonian operator that only considers the pair interactions between nearest-neighbor (NN) atoms is commonly used:

$$E = \frac{1}{2} \sum_{X,Y}^{N_X, N_Y} \varepsilon_{X,Y} M_{X,Y}, \quad (1)$$

where X and Y represent the different atomic species constituting the crystal system, and N_X and N_Y are the number of atoms of every species. Additionally, $\varepsilon_{X,Y}$ is the pair interaction energy matrix between the X and Y atomic species (see details in Table S.M.I in the Supplemental Material [36]), and $M_{X,Y}$ is the neighbor matrix: the matrix element is 1 if the X atomic species is in contact with the Y atomic one; otherwise, the element is equal to 0.

At each step of the kMC trajectory, the system can jump from a given i state to several possible next j states, and the transition rates between the i and all the possible j states are known. The activation energy required for the transition $E_{i \rightarrow j}^{\text{act}}$ is given by

$$E_{i \rightarrow j}^{\text{act}} = \frac{E_i + E_j}{2} - E_i + \varepsilon_o, \quad (2)$$

where ε_o is a constant energy depending on the studied system (for more details, see Ref. [34]), and E_i and E_j are the energies of the i and j states calculated using Eq. (1). Additionally, the associated transition jump rate from the i to the possible j state is given by

$$\omega_j = v_0 \exp\left(-\frac{E_{i \rightarrow j}^{\text{act}}}{k_B T}\right), \quad (3)$$

where j is an index varying from 1 to the final number of available N states, v_0 is the attempt jump frequency, k_B is the Boltzmann constant, and T the simulation temperature (in Kelvin). Then the corresponding N different transition jump rates are summed to yield the total rate constant:

$$\omega_{\text{tot}} = \sum_{j=1}^N \omega_j. \quad (4)$$

In such a way, the transition probability α_j is defined as

$$\alpha_j = \frac{\omega_j}{\omega_{\text{tot}}}. \quad (5)$$

The next j state is chosen among the possible N candidate states; it must fulfill the following condition:

$$\sum_{k=1}^j \alpha_k < r \leq \sum_{k=1}^{j+1} \alpha_k, \quad (6)$$

where r is a generated random number in the range $0 < r < 1$.

Once a new j state is reached, a Monte Carlo step (MCS) is completed, where a MCS corresponds to one attempt exchange per lattice site. The mean residence time Δt_{MCS}^* is the average time in which the system remains in a given state before jumping to the next one; it can be obtained as follows:

$$\Delta t_{\text{MCS}}^* = (\omega_{\text{tot}})^{-1}. \quad (7)$$

For atomic transport assisted by vacancies, a physical time step Δt_{phys} can be defined considering the simulated vacancy concentration C_v^{KMC} and the thermal equilibrium vacancy concentration at the simulated temperature T [33–35]:

$$\Delta t_{\text{phys}} = \Delta t_{\text{MCS}}^* \left(\frac{C_v^{\text{eq}}}{C_v^{\text{KMC}}} \right). \quad (8)$$

In this paper, the kMC computer simulations of solute atom transport in a crystal lattice assisted by a single vacancy were performed using a specific own code named MEGATHERIUM developed in the Python computation language. To extract information from the simulations, an algorithm was implemented to compute the fraction of the physical time f^{at} that each atom species belonging to the alloys studied in this paper (specifically, the superscript *at* corresponds to the Al, Cu, or Mg atoms) spends in contact with the vacancy in a given interval of time τ , where

$$f^{\text{at}} (\%) = 100 \frac{1}{N_{\text{tot}} \tau} \sum_{s=0}^M N_s^{\text{at}} \Delta t_{\text{phys}}, \quad (9)$$

being

$$\tau = \sum_{s=0}^M \Delta t_{\text{phys}}. \quad (10)$$

Additionally, N_s^{at} is the number of atoms of the different atomic species belonging to the alloy in contact with one single vacancy for each MCS step and N_{tot} is the total number of NN atoms to the vacancy. To recognize and classify an agglomeration of solute atoms, that is, solute clusters, a specific algorithm implemented under the frame of the density-based spatial clustering of applications with noise (DBSCAN) algorithm was used [37]. In the developed algorithm, the agglomerates containing three or more solute atoms were considered solute clusters.

On the other hand, to model the structure of the binary or ternary Al-based alloys studied in this paper, different three-dimensional (3D) face-centered cubic (fcc) meshes with L^3 unit cells were considered. Furthermore, to mimic an infinite matrix, periodic boundary conditions in the three possible directions were considered. To simulate the studied alloys, every cell of the 3D mesh was randomly filled with solute atoms in specific amounts, and the remaining cells were filled with aluminum atoms. The single vacancy was simulated by removing 1 Al atom from the mesh, giving an equivalent vacancy concentration of $0.8 \times 10^{-5} \text{at}^{-1}$. Through the simulation, the vacancy was allowed to jump from its position to another of its NNs; 12 in our case due to a fcc structure was used. In this paper, the number of vacancies was considered constant and equal to 1, which means that there exist no sources or sinks of vacancies.

In this paper, kMC simulations were carried out for the following systems: the binary alloy (B alloy) with a composition Al-1.74Cu (at. %) and the ternary alloy (T alloy) with a composition Al-1.74Cu-0.35Mg (at. %). The simulations were performed at 293 and 342 K. These aging temperatures are the same as the experimental ones used to follow the earliest stages of the decomposition of the SSSS of the B and T alloys by means of PALS presented below in Sec. III A. For all modeled alloys, meshes with $L = 50$ containing 1.25×10^5 atoms (the size is $\sim 15 \times 15 \times 15 \text{nm}^3$) were considered. Specifically, for the B alloy, the mesh contains 2175 Cu atoms, and for the T alloy, the mesh contains 2175 Cu and 437 Mg atoms, respectively. To check the reliability of the kMC simulations results, larger 3D fcc meshes ($L = 100$ and 200) were also considered. From our results, nonappreciable differences were obtained when comparing with those obtained using $L = 50$. Moreover, to estimate the uncertainty dispersion associated with the obtained results, each simulation was run five times

III. RESULTS

A. Experimental studies

The experimental results discussed in this section are part of a more general PALS and CBDS investigation carried out by one author of this paper and coworkers at the beginning of this century on the aging kinetics of the binary Al-1.74Cu (at. %) and ternary Al-1.74Cu-0.35Mg (at. %) alloys with or without the addition of 0.1-0.2Ag (at. %) as a microalloying element [8,17,21].

1. Kinetic decomposition

The evolution of the positron lifetime τ with the aging time for the B and T alloys at RT and 342 K are depicted in

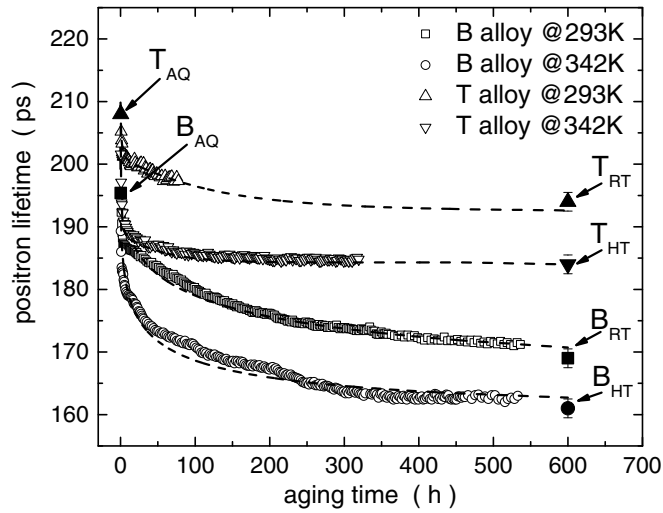


FIG. 1. Positron lifetime evolutions in the binary (B) and ternary (T) alloys as a function of the aging time and temperature after Somoza *et al.* [8,17,21]. Dashed lines are the best-fit curves calculated on the basis of the positron trapping model (see Refs. [17,21]). Labels B_{AQ} , B_{RT} , B_{HT} , T_{AQ} , T_{RT} , and T_{HT} represent the specific aging stages where coincidence Doppler broadening spectroscopy (CDBS) measurements were carried out (see Table I and Ref. [8]).

Fig. 1. In this figure, we present together the positron lifetime vs aging time evolutions for both B and T alloys and for the same aging temperatures which were separately reported in fig. 1 of Ref. [17] and fig. 3 of Ref. [21]. As can be seen, all the curves show the same general feature, that is, a monotonic decreasing behavior of the positron lifetime characterized by an initial rapid drop stage followed by a slower one reaching different asymptotic values depending on the alloy and the aging temperature. In the figure, an increase of the aging temperature leads to a faster and more pronounced τ decrease. Specifically, for the binary alloy, the positron lifetime ~ 195 ps characterizes the initial as-quenched aging stage labeled B_{AQ} . After a long aging time at RT (25 d \equiv 600 h), the stage labeled B_{RT} , the corresponding positron lifetime is ~ 169 ps; for the same aging time but at the higher temperature, τ attains a value of ~ 161 ps (stage labeled B_{HT}).

The τ value at the B_{AQ} stage of the B alloy is higher than that characteristic of positrons annihilated in Cu monovacancies ($\tau_{Cu}^V = 178$ ps [38]), but it is smaller than the typically measured lifetime for positrons annihilated in Al monovacancies ($\tau_{Al}^V = 240$ ps [39]). On the other hand, it is known that, at RT, isolated quenched-in vacancies in pure Al easily migrate, and therefore, they cannot be detected by PALS. Somoza *et al.* [17] reported that the PALS evolution presented in Fig. 1 indicated that positrons became trapped in vacancies associated with Cu atoms (named V-Cu complexes) formed during the quenching process of the B alloy. Moreover, the further τ decrease for increasing aging times and for the two aging temperatures observed in the figure was attributed to a progressive loss of quenched-in vacancies [8,17,21]. This behavior was assigned to the formation of Cu agglomerates assisted by vacancies weakly bonded to the formed solute atom structures. Furthermore, the asymptotic τ value at the B_{HT} stage is very close to that measured for positrons an-

nihilated in pure Al. Such a difference was attributed to the presence of a small amount of vacancy concentration near the lower threshold for the detection of this kind of point defect by the PALS technique.

Regarding the T alloy, in Fig. 1, the as-quenched stage is labeled T_{AQ} , while the longest aging time at the lower temperature is labeled T_{RT} . For the higher aging temperature, this same aging stage is labeled T_{HT} . In the figure, with the addition of a small amount of Mg to the binary alloy, the measured τ values at the two mentioned aging temperatures systematically increase when comparing with those of the B alloy. In Fig. 1, the asymptotic τ values measured in the T alloy for the two aging temperatures are reached at lower aging times than those obtained measuring the B alloy. Somoza *et al.* [21] attributed this behavior to the role of the Mg solute atoms in the T alloy, which stabilize the quenched-in vacancies. Indeed, these authors reported that, after quenching, a higher concentration of vacancies was retained than that detected in the B alloy; thus, vacancies remain bounded to Cu and/or Mg atoms forming solute-vacancy complexes. When aging proceeds, the observed τ decrease was assigned to the loss of a smaller amount of vacancies than those detected in the B alloy; therefore, for long aging times, many vacancies survive as a consequence that they became tightly bonded to the solute clusters.

2. Solute-vacancy interactions

In this paper, the experimental CDBS momentum distributions ρ of the positron annihilation in the B and T alloys aged at RT and 342 K reported in Ref. [8] are now fitted using an improved expression ρ_{fit} proposed later by Dupasquier *et al.* [40]:

$$\rho_{fit} = (1 - F_{trap})\rho_{Al}^{bulk} + F_{trap}(C_{Al}\rho_{Al}^V + C_{Cu}\rho_{Cu}^V + C_{Mg}\rho_{Mg}^V). \quad (11)$$

In this equation, the fitting parameters are the trapping fraction F_{trap} (relative number of positrons trapped and then annihilated in vacancylike defects) and the fractional concentrations of the atomic species belonging to the studied alloys in contact with vacancylike defects C_{Al} , C_{Cu} , and C_{Mg} [for the B alloy, in Eq. (11), $C_{Mg} = 0$]. Furthermore, ρ_{Al}^{bulk} is the momentum distribution for positrons annihilating in the alloy matrix; it is considered the Al bulk momentum distribution measured from a well-annealed high-purity Al since the sensitivity of positrons to a small percentage of substitutional impurities in a SSSS can be neglected. The CDBS momentum distributions ρ_{Al}^V , ρ_{Cu}^V , and ρ_{Mg}^V were obtained measuring severely cold-worked monocrystalline high-purity Al, Cu, and Mg samples. Specifically, the mentioned momentum distributions are due to positron confinement in atomic-sized open volumes, that is, vacancies and vacancylike defects associated with dislocations (in misfit regions). It should be noted that the fractional concentrations (also called contact probabilities) C_i must be interpreted as representing the atomic composition in regions that are in immediate contact with the vacancylike defect where the positron becomes trapped.

To gain information about the chemical nature of the environment probed by the positrons (solute-vacancy interactions), coincidence Doppler broadening distributions were obtained for the specific aging stages labeled B_{AQ} , B_{RT} , B_{HT} ,

TABLE I. Trapping fractions F_{trap} and fractional concentrations C_i of the alloy atomic species in contact with vacancylike defects in the B and T alloys and for the different aging conditions stated in Fig. 1 (see text).

Label	Alloy	Aging condition	Results obtained from the fitting of CDB experimental curves			
			F_{trap} (%) ($\pm 1\%$)	C_{Al} (%) ($\pm 1\%$)	C_{Cu} (%) ($\pm 1\%$)	C_{Mg} (%) ($\pm 1\%$)
B_{AQ}	B	As quenched	26	66	34	
B_{RT}		600 h @293 K	8	32	68	
B_{HT}		600 h @342 K	4	1	99	
T_{AQ}	T	As quenched	47	57	34	9
T_{RT}		600 h @293 K	57	26	65	9
T_{HT}		600 h @342 K	85	14	80	6

T_{AQ} , T_{RT} , and T_{HT} , respectively (see Fig. 1), and then fitted using Eq. (11). From the fittings, the obtained F_{trap} and C_i for the different aging stages of the B and T alloys are reported in Table I.

In the case of the B alloy, in Table I for the as-quenched condition, $\sim 26\%$ of positrons are trapped and then annihilated in vacancylike defects and/or solute-vacancy clusters, while the remaining positrons annihilate in the alloy matrix. This F_{trap} value indicates that, immediately after quenching the SSSS of the alloy, most of the vacancies are lost at RT. However, the C_i values at the stage B_{AQ} indicate that positrons probe, on average, vacancies decorated by 8 Al atoms and 4 Cu solute atoms. When the aging at RT proceeds, the sharp decrease of F_{trap} observed in the B_{RT} stage was attributed to an important loss of positron traps (vacancies); additionally, from the C_i values, a Cu enrichment of the solute-vacancy clusters can be seen. In fact, a $F_{\text{trap}} \sim 8\%$ means that vacancylike defects are in contact with 4 Al atoms and 8 Cu solute atoms. In the table, the increase of the aging temperature to 342 K is reflected in a diminution of F_{trap} until only $\sim 4\%$; that is, $\sim 96\%$ of positrons are annihilated in the alloy matrix, and only a very small fraction of positrons annihilates with vacancies in contact with Cu atoms. The CDBS results reported in Table I also indicate that, at the B_{HT} stage, positron traps are completely surrounded by Cu solute atoms; in fact, $C_{\text{Cu}} \sim 99\%$. This last result made it possible to go deeper into the interpretation of the PALS results obtained for the same aging stage of the binary alloy given in Sec. III A 1. In fact, positrons would mostly prefer to annihilate in effective positron traps of different characteristics from those previously proposed when analyzing PALS data since the vacancy concentration is near the lower threshold for the detection of point defects using the PALS technique.

On the other hand, from the results reported in Table I for the T alloy and for the specific as-quenched stage (T_{AQ}), the Mg addition to the binary alloy practically doubles the F_{trap} value at the same aging stage (B_{AQ}), which means that Mg solute atoms stabilize the quenched-in vacancies. From the C_i values, the solute-vacancy complexes formed during quenching of the SSSS of the ternary alloy are, on average, in contact with 7 Al atoms, 4 Cu, and 1 Mg solute atoms. After 600 h of aging time at RT (T_{RT} stage), F_{trap} increases from 47 to 57%; such an increase can be assigned to the formation of new effective positron traps of a different nature from the vacancy-solute clusters. As described above, this new kind of positron trap has been incipiently observed in the B_{HT}

stage of the binary alloy, despite a very weak signal coming from positrons annihilated in the mentioned positron traps. This issue is discussed in detail in Sec. IV. Moreover, from the evolution of the different C_i values for increasing aging times, positron traps are strongly enriched with Cu solute atoms, while the concentration of Mg solute atoms in contact with such positron traps remains almost constant. Specifically, for the T_{RT} stage, positrons annihilate in traps which are in contact with 3 Al, 8 Cu, and 1 Mg solute atoms. The increase of the aging temperature up to 342 K induces a strong increase of the F_{trap} value, from 57% obtained at the T_{RT} aging stage to 85% at the T_{HT} stage. These results can be attributed to the formation of a higher density of the above denominated effective positron traps. Additionally, it is observed that, at the T_{HT} aging stage, positron traps become even richer in Cu atoms than those detected at the T_{RT} aging stage; in fact, from the corresponding C_i values, on average, positrons are annihilated in effective positron traps that are in contact with 2 Al atoms and 9 Cu and 1 Mg solute atoms.

Based on the results obtained, it is important to point out that the use of the improved expression ρ_{fit} to fit the CDBS data reported in Ref. [8] made it possible to gain information regarding the sites in which positrons become trapped and annihilated.

B. kMC simulations

The results presented in this section are those obtained from kMC simulations of the formation and growth of solute atom clusters assisted by a single vacancy in the binary and ternary alloys at the simulation temperatures of 293 and 342 K. As stated in Sec. II, these temperatures are the same as the aging experimental ones used to follow the early stages of the SSSS decomposition by PALS.

In Sec. III B 1, results about the solute clustering process are presented, while in Sec. III B 2, results on the solute-vacancy interactions are shown.

1. Solute clustering

In Fig. 2, the fractions of solute atoms forming clusters F_C (in %) for the B and T alloys as a function of the physical time t_{phys} are presented. For all the simulated data, the filled areas of the different curves include their associated dispersions delimited by the lower and upper curves.

All curves show a sigmoidal behavior. For the starting point, low F_C values were obtained, that is, ~ 10 and 14%

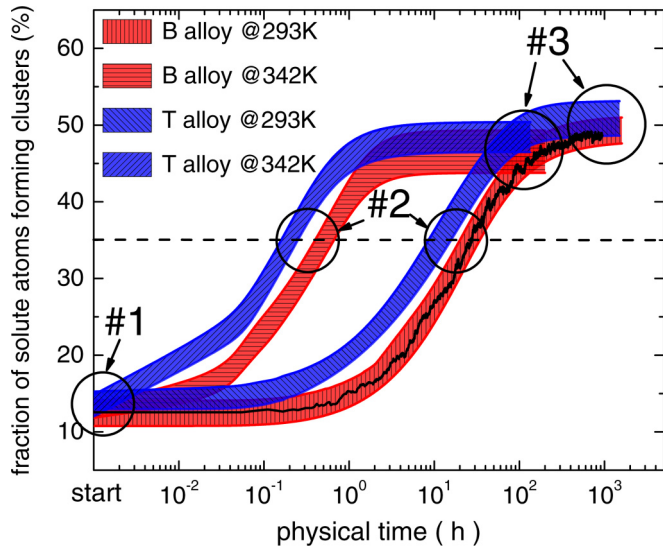


FIG. 2. Fraction of solute atoms forming clusters in the binary and ternary alloys as a function of the physical time and the simulation temperatures. For all the simulated data, the filled areas of the different curves include their associated dispersions (see text). For the sake of clarity, only the average simulated data obtained for the B alloy at 293 K are presented using a solid line. Labels #1, #2, and #3 represent kMC specific stages of the clustering process; that is, #1 is the random starting point, #2 is an intermediate state in which 35% of the solute atoms form clusters, and #3 is the steady state.

for the binary and ternary alloys, respectively. These results indicate that, initially, the randomly distributed solute atoms in the matrix of the alloys form small solute clusters. The curve obtained for the solute atoms forming clusters in the B alloy simulated at 293 K reaches a steady value $\sim 50\%$ for a $t_{\text{phys}} \geq 100$ h. Additionally, for simulations at 342 K, a F_C steady value $\sim 45\%$ is reached for a lower physical time (~ 1 h). Similar trends were observed for the ternary alloy, but in these cases, F_C vs t_{phys} curves are systematically above those obtained for the B alloy (see Fig. 2).

To analyze the results obtained from our simulations, three different stages of the solute clustering process were chosen: (i) Stage #1 corresponds to the starting point; (ii) stage #2 was selected for a specific F_C value representing the regions of the different sigmoidal curves for which the highest F_C growth rates are observed; specifically, $F_C = 35\%$ was chosen which correspond to $t_{\text{phys}} \sim 10$ and 0.1 h for the simulations at 293 and 342 K, respectively; and (iii) stage #3 for which the different F_C reach steady values; specifically, for the simulations at 293 K and for both alloys, it was considered that the steady F_C values were reached for a $t_{\text{phys}} \sim 1000$ h, and in the case of a simulation temperature of 342 K, the same state was reached for $t_{\text{phys}} \sim 100$ h.

In Fig. 3, 3D images of the simulated boxes of the fraction of solute atoms (i.e., Cu atoms) forming clusters in the binary alloy obtained for #1, #2, and #3 solute clustering stages and at the two different simulation temperatures are presented. For the sake of clarity, in the figure, only those Cu atoms forming clusters are shown. The growth of the sizes of Cu clusters as a function of t_{phys} and for the two simulated temperatures is

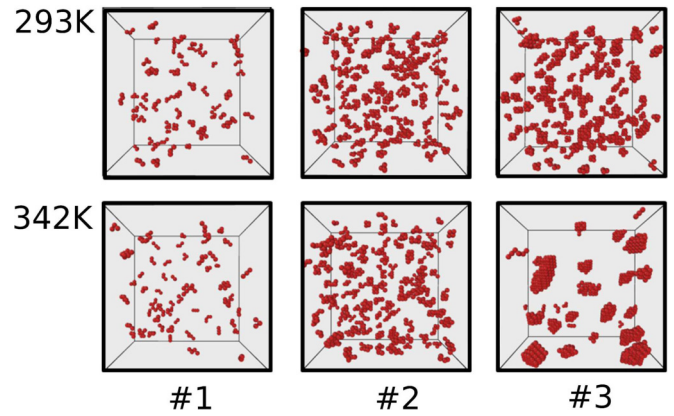


FIG. 3. Three-dimensional (3D) images of the simulated box ($15 \times 15 \times 15 \text{ nm}^3$) of the fraction of solute atoms forming clusters obtained for the binary alloy at different simulation temperatures. For the sake of clarity, only the Cu atoms forming solute clusters are shown. The labels #1, #2 and #3 were defined in Fig. 2.

different, and it is strongly dependent on the temperature; this effect is highly notorious in the case of stage #3.

In Fig. 4, the 3D images of the simulated boxes of the fraction of solute atoms (i.e., Cu and/or Mg) forming clusters in the ternary alloy obtained for #1, #2, and #3 stages and at the two different simulation temperatures are presented. For the sake of clarity, in the figure, only those Cu and/or Mg atoms forming clusters are shown. There is a similar trend in the clustering processes to that observed for the B alloy, and it is also strongly dependent on the simulation temperature. As shown in the figure, pure Cu clusters are jointly formed with Cu-Mg coclusters; our simulations reveal that, despite the initial accidental formation of small pure Mg clusters, for more advanced stages, Mg clusters were not observed.

In Fig. 5, the density of Cu cluster size distributions (Cu-CSD) obtained from the kMC simulations at 293 and 342 K for the B alloy are presented. To identify and quantify the effects of the kinetic simulation on the solute clustering processes, the Cu-CSD in stages #2 and #3 were referred to the

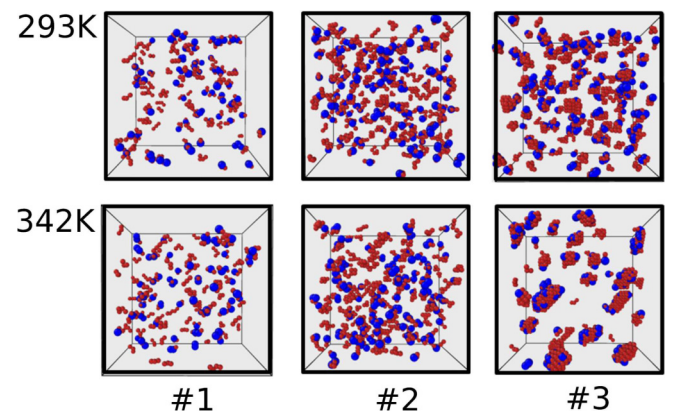


FIG. 4. Three-dimensional (3D) images of the simulation box ($15 \times 15 \times 15 \text{ nm}^3$) obtained for the ternary alloy at different simulation temperatures. For the sake of clarity, only those Cu and Mg atoms forming solute clusters are shown in full red and full blue circles, respectively. The labels #1, #2 and #3 were defined in Fig. 2.

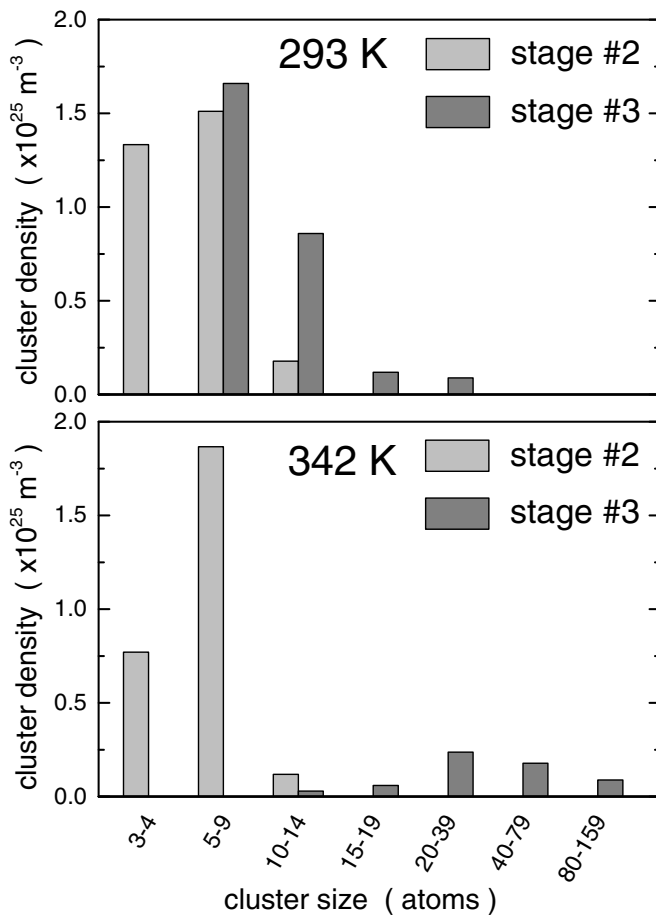


FIG. 5. Density of Cu cluster size distributions as a function of the number of solute atoms (i.e., cluster size) forming Cu clusters for the binary alloy referred to the solute cluster distribution at the initial random state and for simulations at 293 K (top panel) and 342 K (bottom panel). The labels #2 and #3 were defined in Fig. 2. The dispersion associated with the density number of solute clusters is $\pm 5\%$.

Cu-CSD obtained for stage #1. Again, for clarification purposes, the mentioned cluster size distributions are presented for chosen ranges for the number of Cu atoms forming clusters defined between angle brackets as follows: $\langle 3-4 \rangle$, $\langle 5-9 \rangle$, $\langle 10-14 \rangle$, $\langle 15-19 \rangle$, $\langle 20-39 \rangle$, $\langle 40-79 \rangle$, and $\langle 80-159 \rangle$. In the figure, in stage #2 and for 293 K (top panel), the Cu-CSD presents a bimodallike distribution showing its highest value for solute clusters containing $\langle 5-9 \rangle$ Cu atoms. In stage #3, Cu clusters with larger sizes are formed; in this case, a Gaussian-like distribution centered at $\langle 10-14 \rangle$ Cu atoms is observed. For 342 K (bottom panel of Fig. 5), the Cu-CSD in stage #2 presents a derivate normallike distribution with a maximum of solute atoms forming clusters in $\langle 5-9 \rangle$ Cu atoms; this behavior can be attributed to the formation of larger clusters at the expense of those containing $\langle 3-4 \rangle$ Cu atoms. In stage #3, much larger Cu clusters with a wide Cu-CSD centered in $\langle 20-79 \rangle$ Cu atoms are formed. As can be inferred from Fig. 5, the increase of the Cu-CSD at 342 K is accomplished by the coalescence of the smallest Cu clusters obtained for the simulation at 293 K.

In Fig. 6, for the ternary alloy, the density of Cu clusters and Cu-Mg cocluster size distributions (Cu-CSD and Cu-Mg-CSD, respectively) are presented. In this figure, the panels are presented as follows: In the plots labeled (a) and (c), only the Cu-CSD are shown for simulations at 293 and 342 K, respectively. In the plots labeled (b) and (d), only the Cu-Mg-CSD are presented for simulations at the two different temperatures, respectively. As in Fig. 5, the CSD obtained for stages #2 and #3 are referred to the cluster size distribution obtained for stage #1; additionally, the same ranges of the number of solute clusters as those selected for the B alloy were chosen (see above). From the simulations at 293 K, in panel (a) for stage #2, a step function Cu-CSD containing $\langle 3-9 \rangle$ solute atoms is observed; this distribution is almost disappeared for stage #3. Regarding the formation of Cu-Mg coclusters, in panel (b), the CSD results are presented; for stage #2, the Cu-Mg-CSD presents a Gaussian-like distribution centered at $\langle 5-9 \rangle$ Cu-Mg coclusters, and for stage #3, the cluster size distribution is systematically moved toward higher values of Cu-Mg coclusters, specifically $\langle 10-14 \rangle$. In panel (c), the results presented correspond to the Cu-CSD simulated at 342 K; for stage #2, the Cu-CSD presents a Gaussian-like distribution centered at $\langle 3-9 \rangle$ Cu atoms; then for stage #3, the Cu-CSD is completely disappeared. Furthermore, in panel (d) of Fig. 6 (Cu-Mg-CSD at 342 K) for stage #2, the corresponding CSD presents a Gaussian-like distribution centered at $\langle 5-9 \rangle$ Cu-Mg coclusters; and for stage #3, the values of coclusters are strongly shifted to larger Cu-Mg-CSD sizes with a flattened and wide cluster size distribution with a maximum in the range $\langle 40-79 \rangle$.

To show in detail the atomic structure of the Cu-Mg coclusters formed in the ternary alloy, in Fig. 7(a), a zoom of two different representative solute coclusters is shown. To facilitate the comprehension of the cocluster morphology, three different viewpoints are shown. Our simulations indicate that the Cu-Mg coclusters are formed by two nonmixed Cu and Mg solute atoms; an example of the atomic structure of the Cu-Mg coclusters can be seen in the zoomed images presented in the figure.

On the other hand, the analysis of the kMC results obtained for the T alloy indicates that, for increasing simulation times, there is a systematic stoichiometric deviation of the Cu-Mg coclusters when compared with the Mg/Cu ratio equal to 5 of the alloy matrix. This effect is more noteworthy when the simulation temperature is increased. In stage #3, the average Cu/Mg ratio of the coclusters at 293 K is slightly above that corresponding to the matrix; when the simulation temperature is increased in stage #3, the average Cu/Mg ratio is ~ 3 .

2. Solute-vacancy interaction

In Fig. 8, the fraction of the physical time f^{av} that each atom species belonging to the alloys spent in contact with a single vacancy in a given interval of time τ [see Eqs. (9) and (10)] is presented. In the figure, the results obtained for the binary alloy and for simulations carried out at 293 K (top panel) and 342 K (bottom panel) are shown. It is worth mentioning that the chosen ranges of physical times are the same as those of Fig. 2. In Fig. 8, for 293 K, the f^{Cu} values remain approximately constant $\sim 10\%$ until a t_{phys} of ~ 10 h;

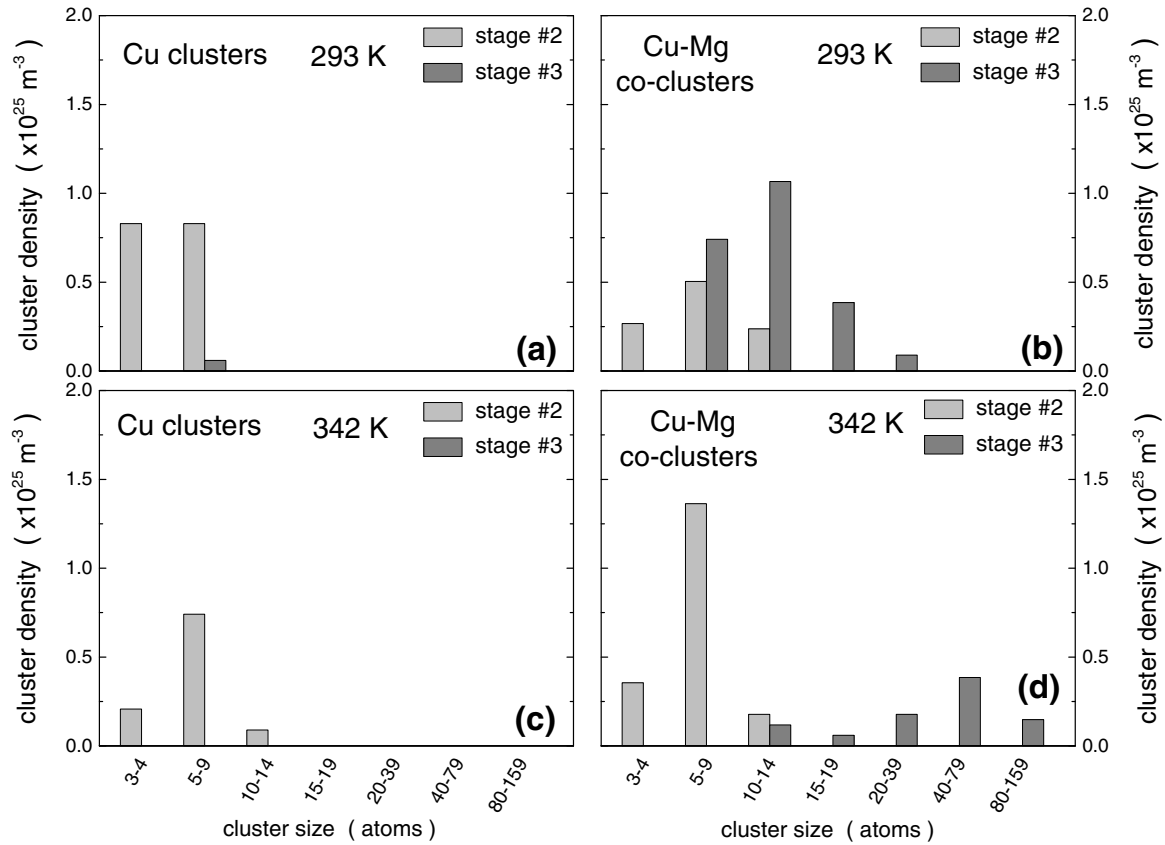


FIG. 6. Density of Cu and Cu-Mg cluster size distributions, referred to the solute cluster distribution as a function of the number of solute atoms (i.e., cluster size) at the initial random state, for the ternary alloy and for simulations at 293 K (top panel) and 342 K (bottom panel). In the plots labeled (a) and (c), only the density of Cu clusters distributions are shown. In the plots labeled (b) and (d), only the density of Cu-Mg cocluster distributions are presented. The labels #2 and #3 were defined in Fig. 2. The uncertainty associated with the density number of solute clusters is $\pm 5\%$.

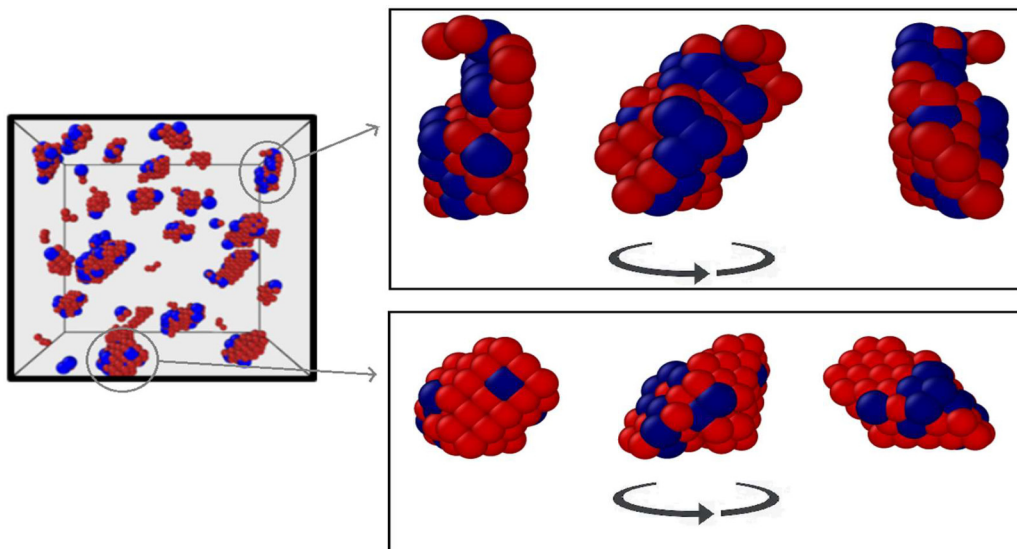


FIG. 7. Three-dimensional (3D) image corresponding to the ternary alloy simulated at 342 K and for stage #3 (see Fig. 4). In the solute clusters, Cu and Mg atoms are shown in full red and full blue circles, respectively. In the right panel, zoomed images of two different representative co-clusters for three different viewpoints are shown (more details are given in the text).

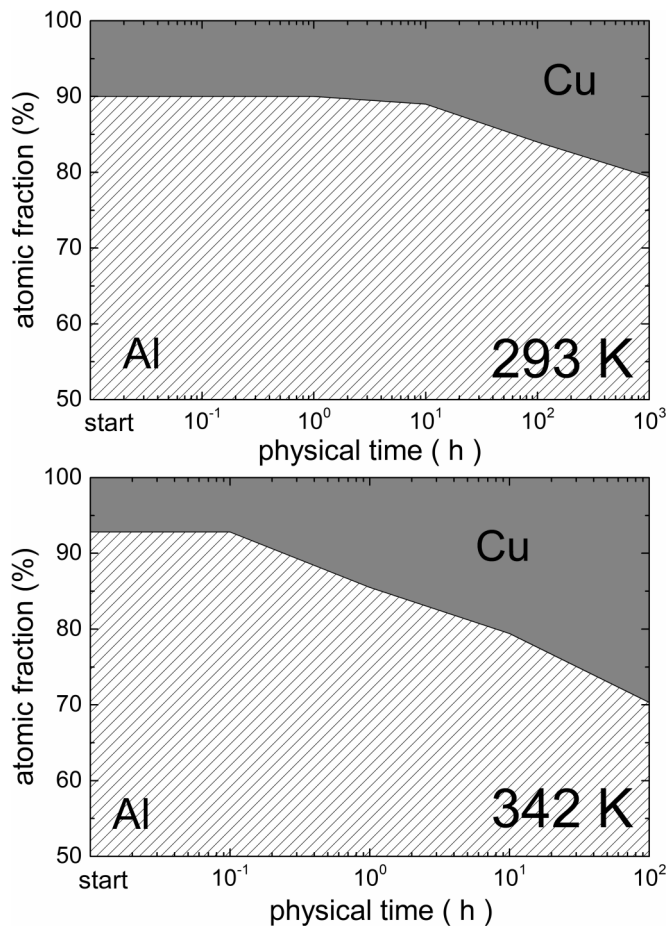


FIG. 8. Fraction of the physical time f^{at} (%) that the Al atoms and Cu solute atoms remain in contact with a vacancy in a given interval of time τ for the binary alloy and for simulations at 293 K (top panel) and 342 K (bottom panel).

then a slight linear increase of this parameter is observed. In fact, for $t_{\text{phys}} = 1000$ h $f^{\text{Cu}} \sim 20\%$. The results obtained from simulations at 293 K and until a physical time of 10 h indicate that, on average, only 1 Cu solute atom and the remaining 11 Al atoms on average are in contact with the single vacancy. In the top panel of Fig. 8, for higher t_{phys} , there is a slight and systematic increase of the average number of Cu atoms in contact with the vacancy; thus, for 1000 h at 293 K (stage #3), on average, there are 2 Cu solute atoms and 10 Al ones in contact with the vacancy. When the simulation temperature is increased to 342 K, the evolution of f^{Cu} vs t_{phys} becomes faster than that obtained for the simulation at 293 K. Thus, until ~ 0.1 h $f^{\text{Cu}} \sim 8\%$; this means that, on average, only 1 Cu solute atom of the 12 atoms surrounding the vacancy is in contact with it. Then for higher physical times, there is an almost linear and sharp f^{Cu} increase. In fact, for $t_{\text{phys}} \sim 100$ h, $f^{\text{Cu}} \sim 30\%$; therefore, on average approximately 4 Cu solute and 8 Al atoms are in contact with the vacancy.

In the case of the ternary alloy and for a simulation temperature at 293 K (see top panel of Fig. 9) and up to $t_{\text{phys}} \sim 0.1$ h, f^{Mg} remains at a similar value to that obtained for the starting point, that is, $\sim 2\%$. For higher physical times and up to 1000 h, f^{Mg} shows a very slight and linear increase (from

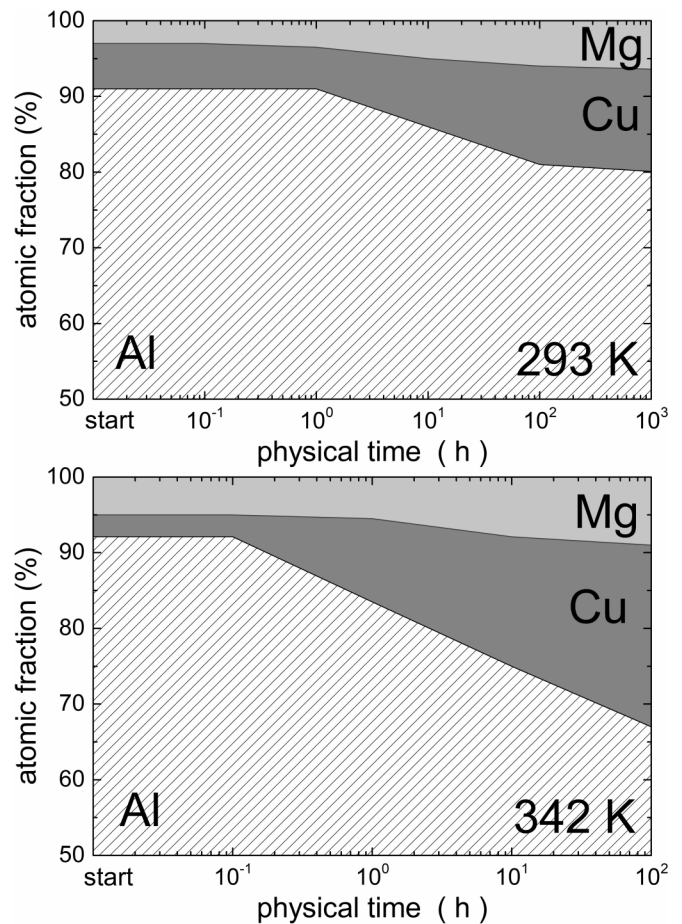


FIG. 9. Fraction of the physical time f^{at} (%) that the Al atoms and Cu and/or Mg solute atoms remains in contact with a vacancy in a given interval of time τ for the ternary alloy and for simulations at 293 K (top panel) and 342 K (bottom panel).

~ 2 to $\sim 6\%$). For Cu solute atoms and for the early simulation stages ($0 \leq t_{\text{phys}} \leq 0.1$ h), f^{Cu} values remain constant. In the figure, for higher physical times, there is a systematic f^{Cu} increase reaching a final value of $\sim 13.5\%$ for $t_{\text{phys}} = 1000$ h. The increase of the simulation temperature is reflected in an acceleration of the described processes.

The results presented in Figs. 8 and 9 arise as a cumulative average of the fraction of the physical time that the atom species of the alloys spend in contact with a single vacancy during the total time of the kMC simulations at 293 and 342 K and for the two studied alloys. Under this frame, the t_{phys} ranges chosen to calculate the different f^{at} were, in the case of the simulations at 293 K, from 0 to 0.1 h, 0 to 1 h, 0 to 10 h, 0 to 100 h, and 0 to 1000 h. Specifically, at 342 K the maximum t_{phys} chosen for the simulations was 100 h.

Briefly, the results presented in Figs. 8 and 9 made it possible to understand how the vacancy interacts with the different atomic species to build the solute clusters. Additionally, the increase of the simulation temperature accelerates this process.

IV. OVERALL DISCUSSION

The main experimental PALS and CDBS results presented in Sec. III A are summarized according to the alloy studied as follows.

For the binary alloy, the results obtained show that, after quenching the SSSS, quenched-in vacancies associated with Cu solute atoms are formed. Then during aging, such quenched-in vacancies are progressively lost when forming Cu clusters assisted by vacancies which are weakly bonded to the formed solute agglomerates. This process accelerates when the aging temperature is increased. In the last stage of the aging process, PAS (PALS and CDBS) results indicate that there are a few solute clusters entirely composed of Cu atoms acting as effective positron traps.

PAS results obtained for the ternary alloy indicate that the mechanism of solute-vacancy interaction and solute clustering are completely different from those observed for the binary alloy. This behavior was attributed to the role of Mg atoms which stabilize the quenched-in vacancies since they are tightly bonded to those solute atoms forming Cu-Mg coclusters. When aging proceeds, vacancies remain bonded to Cu and/or Mg atoms forming solute-vacancy clusters and Cu-Mg coclusters.

Additionally, from the evolution of the F_{trap} values obtained for the binary and ternary alloys (see Table I), it could be concluded that another kind of effective positron trap is formed in the alloys, that is, vacancy-free solute clusters. Additionally, it was found that this phenomenon is more noticeable for the ternary alloy. In the case of Cu-Mg coclusters, it was revealed that the mentioned coclusters are significantly richer in Cu than in Mg atoms. This effect is more significant for the higher aging temperature.

From the theoretical point of view, Kuriplach *et al.* [41] studied positron annihilation in Al-Cu age-hardenable alloys for several kinds of Cu clusters embedded in an Al matrix. To calculate positron lifetimes in the matrix or in the Cu nanoclusters, these authors employed *ab initio* calculations based on the concept of the positron affinity A_+ defined as the sum of the internal electron and positron chemical potentials (see Ref. [41]). In their paper, the authors demonstrated that A_+ reflects the preference of the positron for different components in heterostructures made of different materials, and they also reported that positrons have a preference between the host matrix and precipitates formed in the alloys.

In Sec. II of the Supplemental Material [36], we report, for the binary and ternary alloys, results obtained using *ab initio* calculations of the localization of the positron wave functions and their respective positron lifetimes. Toward this aim, we considered several configurations of Cu solute clusters and Cu-Mg coclusters embedded in an Al matrix. The results obtained give evidence of why vacancy-free solute clusters act as effective positron traps, and they are in total agreement with those reported by Kuriplach *et al.* [41]. Puska *et al.* [42] reported that, when comparing vacancy-free solute clusters with vacancy-related defects, the first type of positron trap is less effective than the second one; additionally, the effectiveness of the vacancy-free solute clusters depends on their composition. Such clusters can trap positrons, provided their sizes are above a critical size which depends on the

TABLE II. Values of the positron affinities A_+ of each atom species forming the alloys, differences ΔA_+ from between the A_+ value of the host matrix and the corresponding value to each solute species, and the critical radius r_c of the vacancy-free solute clusters atoms [obtained using Eq. (12)] formed in the binary Al-1.74Cu (at. %) and ternary Al-1.74Cu-0.35Mg (at. %) alloys.

Element	A_+ (eV)	ΔA_+ (eV)	r_c (nm)
Al	-4.41	0	-
Cu	-4.81	0.40	0.49
Mg	-6.18	1.77	0.23

positron affinity of the involved solute elements. Additionally, the authors also reported that, to become an effective positron trap, vacancy-free solute clusters must be larger than a critical size, whose radius r_c (in nm) can be calculated as follows:

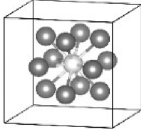
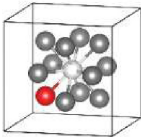
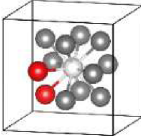
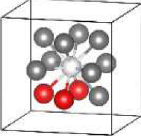
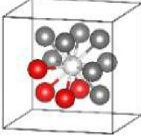
$$r_c \approx \frac{0.58 a_o}{\sqrt{\Delta A_+}} \approx \frac{0.31}{\sqrt{\Delta A_+}}, \quad (12)$$

where a_o is the Bohr radius, and ΔA_+ (eV) is the difference between the affinity of the host matrix (Al in our case) and the solute atoms forming clusters. The corresponding A_+ values of the atomic species of our binary and ternary alloys were reported in Ref. [42]; they are listed in Table II.

Considering an Al fcc crystal lattice (lattice parameter = 4.05 Å) containing different amounts of solute atoms, independently of the chemical element, in substitutional positions of the lattice, we have geometrically estimated different solute cluster radii; for example, a cluster formed by 13 solute atoms has a radius ~ 0.3 nm; for a cluster containing 19 solute atoms, its radius is ~ 0.4 nm; and a cluster with 42 solute atoms has a radius ~ 0.5 nm. Thus, for Cu atoms, the critical radius calculated using Eq. (12) is $r_c \approx 0.49$ nm, and for Mg ones, $r_c \approx 0.23$ nm (see Table II). From these results, it can be concluded that, to become an effective positron trap, a vacancy-free Cu cluster must contain >40 Cu atoms, while a vacancy-free Mg cluster must be formed by >9 Mg atoms.

On the other hand, from the kMC calculations for the binary alloy at 293 K and long physical times (stage #3), the results obtained revealed that the Cu solute clusters have 9 Cu atoms on average which are not large enough to constitute an effective positron trap. On the contrary, when the temperature is increased up to 342 K, there is an important increase of the solute clusters having up to 40 Cu atoms on average; in this case, such Cu clusters become effective positron traps. In the ternary alloy, results of the kMC calculations at 293 K and for long physical times indicate that a Cu-Mg cocluster contains 12 solute atoms on average, 9 Cu atoms and 3 Mg ones; in such a case, only those Co-Mg coclusters having a larger number of solute atoms than the average could act as effective positron traps [see Fig. 6(b)]. For the higher aging temperature and long physical times, the average number of solute atoms forming Cu-Mg coclusters drastically increased up to 72 atoms, 55 Cu atoms and 17 Mg ones; under this scenario, almost all Co-Mg clusters become effective positron traps [see Fig. 6(d)]. Summarizing, the use of kMC calculations in this paper made it possible to precisely determine the sizes and the respective compositions of the solute clusters

TABLE III. Fraction of the physical time f^{at} (%) that, for the established time ranges, each atom species belonging to the alloy Al-1.74Cu (at. %) at 293 K remains in contact with a vacancy in a given interval of time τ . Empty cells indicate that, for certain vacancy neighborhood, f^{at} values are $<10\%$, while for the gray cells, $f^{at} = 0$.

Vacancy neighborhood		Physical time ranges (h)			
		0.1 to 1	1 to 10	10 to 100	100 to 1000
Al ₁₂ -V		11%	10%	10%	13%
Al ₁₁ -V-Cu ₁		73%	64%	29%	16%
Al ₁₀ -V-Cu ₂		16%	20%	28%	21%
Al ₉ -V-Cu ₃				21%	26%
Al ₈ -V-Cu ₄					13%

and Cu-Mg coclusters to become effective positron traps in the binary and ternary alloys.

There is still a more important contribution of kMC calculations which allows us to describe and comprehend (i) how the solute-vacancy interaction is and (ii) the mechanisms involved in the transport of solute atoms assisted by vacancies to form and grow solute clusters.

The kMC key parameter chosen in this paper to describe the abovementioned processes is the fraction of the physical time f^{at} [defined in Eq. (9)] that each atom species of the alloys spends in contact with a single vacancy in a given interval of time τ . A first approach to analyze the vacancy interaction with each neighboring atom species was given in Sec. III B 2 (see Figs. 8 and 9). To go deeper into the comprehension of this subject, in this section, f^{at} values are

presented considering the different possible configurations in which a single vacancy is in contact with the 12 NN atom species in a fcc structure.

In Tables S.M. IV–S.M. VII in the Supplemental Material [36], the complete set of f^{at} values obtained for different vacancy neighborhoods in the binary and ternary alloys and the two simulation temperatures are reported. To facilitate the interpretation and discussion of these kMC results, in Tables III–VI, the more significant cases are presented. Additionally, only the f^{at} values $>10\%$ are presented. Furthermore, in the tables, the f^{at} values obtained in the range $0 \leq t_{\text{phys}} \leq 0.1$ h are not shown because this interval of time is very short, and consequently, the accumulated statistic from the calculations is low. In all these tables, in the column named vacancy neighborhood, a graphical

TABLE IV. Fraction of the physical time f^{at} (%) that, for the established time ranges, each atom species belonging to the alloy Al-1.74Cu (at. %) at 342 K remains in contact with a vacancy in a given interval of time τ . Empty cells indicate that, for certain vacancy neighborhood, f^{at} values are $<10\%$, while for the gray cells, $f^{at} = 0$.

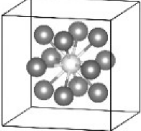
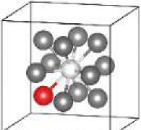
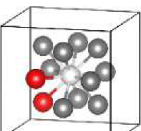
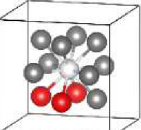
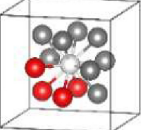
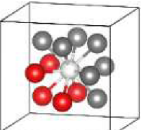
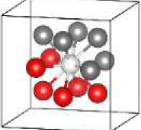
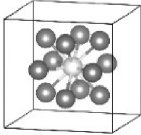
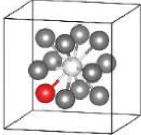
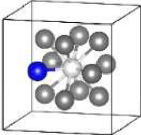
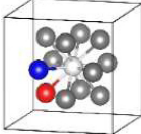
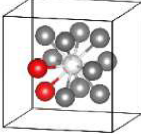
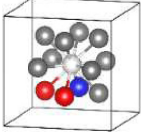
Vacancy neighborhood		Physical time ranges (h)		
		0.1 to 1	1 to 10	10 to 100
Al ₁₂ -V		10%	11%	11%
Al ₁₁ -V-Cu ₁		41%	21%	10%
Al ₁₀ -V-Cu ₂		25%	20%	10%
Al ₉ -V-Cu ₃		13%	23%	20%
Al ₈ -V-Cu ₄		11%	12%	15%
Al ₇ -V-Cu ₅				19%
Al ₆ -V-Cu ₆				11%

TABLE V. Fraction of the physical time f^{at} (%) that, for the established time ranges, each atom species belonging to the alloy Al-1.74Cu-0.35Mg (at. %) at 293 K remains in contact with a vacancy in a given interval of time τ . Empty cells indicate that, for certain vacancy neighborhood, f^{at} values are <10%, while for the gray cells, $f^{at} = 0$.

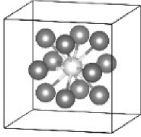
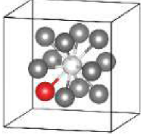
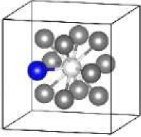
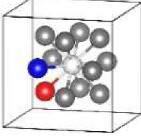
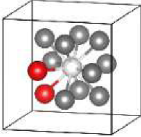
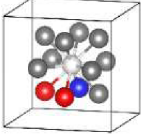
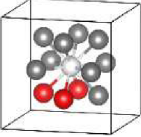
Vacancy neighborhood	Physical time ranges (h)			
	0.1 to 1	1 to 10	10 to 100	100 to 1000
Al ₁₂ -V 				
Al ₁₁ -V-Cu ₁ 	49%	28%	13%	11%
Al ₁₁ -V-Mg ₁ 	40%	27%	13%	11%
Al ₁₀ -V-Cu ₁ Mg ₁ 		18%	15%	10%
Al ₁₀ -V-Cu ₂ 			10%	12%
Al ₉ -V-Cu ₂ Mg ₁ 			11%	13%

scheme of each configuration with its chemical compositions is shown; for example, Al₁₁-V-Cu₁ represents the vacancy (V) surrounded by 11 Al atoms and 1 Cu solute atom, and Al₉-V-Cu₂Mg₁ represents the vacancy in contact with 9 Al atoms and a cocluster formed by 2 Cu and 1 Mg solute atoms.

In Table III, the different f^{at} values correspond to the binary alloy and for kMC simulations at 293 K. In the case of the vacancy surrounded by 12 Al atoms and for the t_{phys}

ranges between 0.1 and 10 h and 10 and 100 h, on average, the vacancy spends $\sim 11\%$ of its physical time in contact with Al atoms; these f^{at} values slightly increase for the longest time range (100 to 1000 h). It must be noted that, under this scenario, the parameter f^{at} could be ascribed to the time spent by the vacancy-searching solute atoms, which is Cu for the B alloy. The meaning of this parameter is still the same for the vacancy surrounded by 12 Al atoms in the ternary alloy. In the remaining physical times, the vacancy is involved in

TABLE VI. Fraction of the physical time f^{at} (%) that, for the established time ranges, each atom species belonging to the alloy Al-1.74Cu-0.35Mg (at. %) at 342 K remains in contact with a vacancy in a given interval of time τ . Empty cells indicate that, for certain vacancy neighborhood, f^{at} values are <8%, while for the gray cells, $f^{at} = 0$. * See text.

Vacancy neighborhood	Physical time ranges (h)		
	0.1 to 1	1 to 10	10 to 100
Al ₁₂ -V 			
Al ₁₁ -V-Cu ₁ 	19%		
Al ₁₁ -V-Mg ₁ 	12%		
Al ₁₀ -V-Cu ₁ Mg ₁ 	25%		
Al ₁₀ -V-Cu ₂ 	14%		
Al ₉ -V-Cu ₂ Mg ₁ 	17%	11%	8%*
Al ₉ -V-Cu ₃ 		11%	8%*

a dynamic process including the transport of solute atoms to form solute clusters in the binary as well as in the ternary alloy. In this process, the single vacancy acts as a carrier of the different solute atoms (Cu and/or Mg).

In Table III, when in the B alloy the vacancy is surrounded by 11 Al atoms and 1 Cu solute atom and until 8 Al atoms and 4 Cu ones, the percentage of time that the vacancy spends in contact with Cu solute atoms strongly decreases. Specifically, for $0.1 \leq t_{\text{phys}} \leq 1$ h, the vacancy is mainly in contact with 1 ($f^{\text{at}} = 73\%$) or 2 ($f^{\text{at}} = 16\%$) Cu atoms. For higher time ranges, the vacancy progressively spends more time in contact with an increasing number of solute atoms, and therefore, the corresponding f^{at} values become more distributed.

The increase of the simulation temperature for the B alloy does not change the percentage of time that the vacancy spends in contact with 12 Al atoms, but our results indicate that the encountering of the vacancy with different amounts of solute atoms is favored (see Table IV). In fact, in the physical time range between 10 and 100 h, the vacancy is progressively in contact with 1 until 6 Cu atoms; hence, at maximum, the vacancy is in contact with 6 Al and 6 Cu atoms. Thus, it could be assumed that the vacancy should spend a fraction of time in the boundary between Cu solute clusters and the alloy matrix. Consequently, the vacancy not only acts as a carrier of solute atoms, but also, it is responsible for the formation of solute clusters fulfilling the vacancy pump model [8,43,44].

For the ternary alloy, the different f^{at} values obtained for the kMC simulations at 293 K are presented in Table V. In the case of the single vacancy surrounded by 12 Al atoms, for all t_{phys} , the percentage of time spent by the vacancy in contact with Al atoms is almost constant ($\sim 5\%$, see Table S.M. VI in the Supplemental Material [36]); this f^{at} value is lower than that obtained for the binary alloy. When compared with the B alloy, the value $f^{\text{at}} \sim 5\%$ obtained for the T alloy can be assigned to two factors: (i) More solute atoms, mainly Mg ones, are available in the alloy matrix; therefore, the vacancy spends less time searching them; and (ii) since the interaction between the vacancy and Mg atoms is more favorable than that with Cu or Al atoms (see values of the pair interaction energies between the vacancy and the atom species presented in Table S.M. I in the Supplemental Material [36]), the vacancy proportionally spends more time in contact with Mg atoms. In the remaining percentage of physical times, the vacancy is involved in a dynamic process including the transport of solute atoms to form solute clusters and/or Cu-Mg coclusters. In Table V, in the range $0.1 \leq t_{\text{phys}} \leq 1$ h, the vacancy spends almost half of the time in contact with a single Cu solute atom and $\sim 40\%$ with a single Mg atom. It is important to point out that, despite the Cu/Mg ratio being ~ 5 , the f^{at} values either for Cu or Mg solute atoms are similar. This result is a clear signal that the vacancy strongly prefers to interact with Mg rather than with Cu atoms. For higher physical time ranges, the vacancy is in contact with more Cu and/or Mg solute atoms; therefore, in Table V, larger solute clusters with different configurations are formed.

Furthermore, for the ternary alloy, the increase of the simulation temperature up to 342 K does not change the percentage of time that the vacancy spends in contact with 12 Al atoms ($\sim 5\%$, see Table S.M. VII in the Supplemental Material [36]).

In Table VI, during the shorter t_{phys} range ($0.1 \leq t_{\text{phys}} \leq 1$ h), the vacancy spends a time roughly equally distributed with a solute atom (Cu or Mg), a Cu-Mg solute cocluster, and a solute cocluster formed by 2 Cu and 1 Mg atoms. By increasing t_{phys} ranges, the vacancy does not significantly interact with the simplest solute cluster configurations. Specifically, in the range $1 \leq t_{\text{phys}} \leq 10$ h, the vacancy spends a very short fraction of time in contact with $\text{Al}_6\text{-V-Cu}_5\text{Mg}_1$ and $\text{Al}_6\text{-V-Cu}_4\text{Mg}_2$ coclusters, and in the remaining time, the vacancy is in contact with simpler solute cluster configurations; more detailed information is given in Table S.M. VII in the Supplemental Material [36]. For the last physical time range ($10 \leq t_{\text{phys}} \leq 100$ h), the last mentioned behavior is still more notorious; in fact, the highest percentage of time that the vacancy spends in contact with solute atoms ($\sim 8\%$) corresponds to configurations formed by 3 Cu atoms or the cocluster formed by 2 Cu and 1 Mg atoms. The remaining time the vacancy is in contact with different solute clusters or cocluster configurations; from our simulations, the more complex configurations are $\text{Al}_3\text{-V-Cu}_6\text{Mg}_3$ and $\text{Al}_3\text{-V-Cu}_5\text{Mg}_4$ (for more details, see Table S.M. VII in the Supplemental Material [36]).

As discussed above in the case of the binary alloy, for the ternary alloy, the single vacancy should spend a fraction of time in the boundary between more complex configurations of Cu and/or Mg solute clusters and/or Cu-Mg coclusters and in the alloy matrix. In the same way as for the binary alloy, in the T alloy, the transport of solute atoms assisted by vacancies is framed into the vacancy pump model [8,43,44].

As mentioned above for the binary alloy, in the T alloy, the vacancy not only acts as a carrier of solute atoms, but also, it is responsible for the formation of Cu and/or Mg solute clusters and Cu-Mg solute coclusters fulfilling the vacancy pump model.

V. CONCLUSIONS

The results reported in this paper, obtained through the convergence between positron experimental techniques and a modeling approach through kMC simulations, represent an outstanding case in the search for a detailed description of the fundamental mechanisms responsible for the solute-vacancy interaction and solute atom diffusion assisted by vacancies responsible for the solute clustering and related phenomena. This paper is focused on the study of the early aging stages of the precipitation kinetics of the alloys Al-1.74Cu (at. %) and Al-1.74Cu-0.35Mg (at. %).

Our results point out that, in a thermally activated process, the supersaturated solid solution quenched-in vacancies not only act as a carrier of solute atoms, but they are also responsible for the formation and growth of solute clusters and their energetic stabilization fulfilling the vacancy pump model. The aging temperatures chosen were low enough to avoid the formation of more stable nanostructures.

PAS experimental data reported by Somoza *et al.* [8,17,21] were fitted using an improved model that made it possible to gain information regarding the sites in which positrons become trapped and annihilated. Specifically, using PAS techniques, information was obtained on the vacancy-type defects and, through them, on their chemical environments of the species of atoms belonging to the alloy.

The use of an implementation of kMC simulations allowing us to directly link the calculated kMC results with the experimental PAS ones made it possible to quantify the fraction of time that a vacancy spends searching and transporting solute atoms to build clusters. It is worth mentioning that kMC results not only provide specific information on the solute clustering, but they also put a magnifying glass on the roam of vacancies from the search for solute atoms followed by their transport to form and grow Cu and/or Mg solute clusters and Cu-Mg solute coclusters. Our results also indicate that vacancies remain bonded to Cu and/or Mg atoms forming solute-vacancy clusters.

On the other hand, it was revealed that the addition of Mg as a minor alloying element to the binary alloy induces remarkable changes in the solute clustering process and in the mechanisms involved in the solute-vacancy interactions. Additionally, the obtained results indicate that, together with the Cu and/or Mg atoms forming solute-vacancy clusters, the solute atoms transported by vacancies progressively form Cu-Mg coclusters containing different amounts of nonmixed solute atoms.

Summarizing, the results reported in this paper, obtained from the combined use of positron experimental techniques and kMC simulations, represent a leading case to extend the current knowledge on the fundamental mechanisms operating during aging in simple binary and ternary age-hardenable Al-based alloys to more complex metallic systems [48].

ACKNOWLEDGMENTS

The authors acknowledge funding from ANPCyT (Grant No. PICT-2015-1832), Comisión de Investigaciones Científicas de la Provincia de Buenos Aires (Argentina) and Secretaría de Ciencia, Arte y Tecnología SECAT-UNCPBA (Argentina). The authors gratefully acknowledge Emeritus Professor Ian J. Polmear (Department of Materials Science and Engineering, Monash University, Australia) for encouraging us to carry out this challenging study. We also deeply thank him for his comments about our manuscript, which allowed us to enrich the discussion of the results presented in this paper.

-
- [1] I. J. Polmear, *Light Alloys: From Traditional Alloys to Nanocrystals* (Oxford, Elsevier, 2006).
- [2] I. Polmear, D. StJohn, J. F. Nie, and M. Qian, *Light Alloys: Metallurgy of the Light Metals* (Butterworth-Heinemann, Oxford, 2017).
- [3] B. Gault, M. P. Moody, J. M. Cairney, and S. P. Ringer, *Atom Probe Microscopy* (Springer Science & Business Media, New York, 2012), Vol. 160.
- [4] B. Gault, A. Chiramonti, O. Cojocar-Mirédin, P. Stender, R. Dubosq, C. Freysoldt, S. K. Makineni, T. Li, M. Moody, and J. M. Cairney, *Nat. Rev. Methods Primers* **1**, 51 (2021).
- [5] A. Dupasquier, G. Kögel, and A. Somoza, *Acta Mater.* **52**, 4707 (2004).
- [6] A. Somoza and A. Dupasquier, in *Fundamentals of Aluminium Metallurgy*, edited by R. N. Lumley (Woodhead Publishing, Cambridge, 2011), pp. 386–421.
- [7] G. Dlubek, O. Kabisch, O. Brümmer, and H. Löffler, *Phys. Stat. Solidi A* **55**, 509 (1979).
- [8] A. Somoza, M. P. Petkov, K. G. Lynn, and A. Dupasquier, *Phys. Rev. B* **65**, 094107 (2002).
- [9] T. Honma, S. Yanagita, K. Hono, Y. Nagai, and M. Hasegawa, *Acta Mater.* **52**, 1997 (2004).
- [10] J. Čížek, O. Melikhova, I. Prochazka, J. Kuriplach, I. Stulikova, P. Vostry, and J. Faltus, *Phys. Rev. B* **71**, 064106 (2005).
- [11] M. Kaiser, P. Nambissan, M. Banerjee, A. Sachdeva, and P. Pujari, *J. Mater. Sci.* **42**, 2618 (2007).
- [12] R. Ferragut, A. Dupasquier, C. E. Macchi, A. Somoza, R. N. Lumley, and I. J. Polmear, *Scr. Mater.* **60**, 137 (2009).
- [13] G. Dlubek, *Mater. Sci. Forum* **13-14**, 11 (1987).
- [14] R. Krause, G. Dlubek, and O. Brümmer, in *European Meeting on Positron Studies of Defects*, edited by G. Dlubek, O. Brümmer, G. Brauer, and K. Hennig (Martin Luther University, Halle, 1987), Vol. 1, No. 2, PL 7.
- [15] *Positron in Solids*, edited by P. Hautojärvi, in Topics in Current Physics (Springer-Verlag, Berlin, Heidelberg, New York, 1979), Vol. 12.
- [16] A. Dupasquier, N. De Diego, P. Folegati, and A. Somoza, *J. Phys. Condens. Matter.* **10**, 10409 (1998).
- [17] A. Somoza, A. Dupasquier, I. J. Polmear, P. Folegati, and R. Ferragut, *Phys. Rev. B* **61**, 14464 (2000).
- [18] C. Macchi, A. Tolley, R. Giovachini, I. J. Polmear, and A. Somoza, *Acta Mater.* **98**, 275 (2015).
- [19] R. Ferragut, A. Somoza, and A. Dupasquier, *J. Phys. Condens. Matter.* **10**, 3903 (1998).
- [20] G. Dlubek, P. Lademann, H. Krause, S. Krause, and R. Unger, *Scr. Mater.* **39**, 893 (1998).
- [21] A. Somoza, A. Dupasquier, I. J. Polmear, P. Folegati, and R. Ferragut, *Phys. Rev. B* **61**, 14454 (2000).
- [22] T. E. M. Staab, E. Zschech, and R. Krause-Rehberg, *J. Mater. Sci.* **35**, 4667 (2000).
- [23] Y. Nagai, M. Murayama, Z. Tang, T. Nonaka, K. Hono, and M. Hasegawa, *Acta Mater.* **49**, 913 (2001).
- [24] T. E. M. Staab, R. Krause-Rehberg, U. Hornauer, and E. Zschech, *J. Mater. Sci.* **41**, 1059 (2006).
- [25] M. Liu, J. Čížek, C. S. Chang, and J. Banhart, *Acta Mater.* **91**, 355 (2015).
- [26] M. Elsayed, A. M. Ibrahim, T. E. M. Staab, and R. Krause-Rehberg, *J. Phys.: Condens. Matter* **33**, 435401 (2021).
- [27] F. James, *Rep. Prog. Phys.* **43**, 1145 (1980).
- [28] A. F. Voter, in *Radiation Effects in Solids*, edited by K. E. Sickafus, E. A. Kotomin, and B. P. Uberuaga (Springer, Dordrecht, 2007), Vol. 235, pp. 1–23.
- [29] A. Chatterjee and D. G. Vlachos, *J. Comput. Aided Mol. Des.* **14**, 253 (2007).
- [30] K. Reuter and M. Scheffler, *Phys. Rev. B* **73**, 045433 (2006).
- [31] M. A. Quiroga and A. A. Franco, *J. Electrochem. Soc.* **162**, E73 (2015).
- [32] A. Deschamps and C. R. Hutchinson, *Acta Mater.* **220**, 117338 (2021).
- [33] G. Sha and A. Cerezo, *Acta Mater.* **53**, 907 (2005).
- [34] F. De Geuser, B. M. Gable, and B. C. Muddle, *Philos. Mag.* **91**, 315 (2011).

- [35] Z. Liang, C. S. T. Chang, C. Abromeit, J. Banhart, and J. Hirsch, *Int. J. Mater. Res.* **103**, 980 (2012).
- [36] See Supplemental Material at <http://link.aps.org/supplemental/10.1103/PhysRevMaterials.6.033603> for additional and detailed information regarding kMC simulations and theoretical information on the characteristic parameters of the positron-electron annihilation process obtained using *ab initio* calculations, including Refs. [45–48].
- [37] E. Schubert, J. Sander, M. Ester, H-P. Kriegel, and X. Xu, *ACM Trans. Database Syst.* **42**, 1 (2017).
- [38] T. Hehenkamp, T. Kurschat, and W. Luhr-Tanck, *J. Phys. F: Met. Phys.* **16**, 981 (1986).
- [39] H. Hakkinen, S. Mäkinen, and M. Manninen, *Phys. Rev. B* **41**, 12441 (1990).
- [40] A. Dupasquier, R. Ferragut, M. M. Iglesias, M. Massazza, G. Riontino, P. Mengucci, C. Macchi, and A. Somoza, *Philos. Mag. A* **87**, 3297 (2007).
- [41] J. Kuriplach, F. Becvar, J. Cizek, and I. Prochazka, *Mater. Sci. Forum* **445-446**, 132 (2004).
- [42] M. J. Puska, P. Lanki, and R. M. Nieminen, *J. Phys. Condens. Mater.* **1**, 6081 (1989).
- [43] L. A. Girifalco and H. Herman, *Acta Metall.* **13**, 583 (1965).
- [44] M. Ipohorski and A. F. Bonfiglioli, *Acta Metall.* **18**, 281 (1970).
- [45] M. J. Puska and R. M. Nieminen, *Rev. Mod. Phys.* **66**, 841 (1994).
- [46] T. Torsti, T. Eirola, J. Enkovaara, T. Hakala, P. Havu, V. Havu, T. Höynälänmaa, J. Ignatius, M. Lyly, I. Makkonen, T. T. Rantala, J. Ruokolainen, K. Ruotsalainen, E. Räsänen, H. Saarikoski, and M. J. Puska, *Phys. Status Solidi B* **243**, 1016 (2006).
- [47] E. Boronski and R. M. Nieminen, *Phys. Rev. B.* **34**, 3820 (1986).
- [48] J. M. Campillo, E. Ogando, and F. Plazaola, *J. Phys.: Condens. Matter* **19**, 176222 (2007).